Journal of Alloys and Compounds 819 (2020) 152959

Contents lists available at ScienceDirect

Journal of Alloys and Compounds

journal homepage: http://www.elsevier.com/locate/jalcom

Superconductivity of $Y_5Rh_6Sn_{18}$; Coexistence of the high temperature thermal lattice relaxation process and superconductivity

A. Ślebarski [a, b, *], P. Zajdel [a], M.M. Maśka [a], J. Deniszczyk [c], M. Fijałkowski [a]

[a] Institute of Physics, University of Silesia in Katowice, 75 Pułku Piechoty 1, 41-500, Chorzów, Poland
[b] Centre for Advanced Materials and Smart Structures, Polish Academy of Sciences, Okólna 2, 50-950, Wrocław, Poland
[c] Institute of Materials Engineering, University of Silesia in Katowice, 75 Pułku Piechoty 1A, 41-500, Chorzów, Poland

ARTICLE INFO

Article history:
Received 14 August 2019
Received in revised form
6 November 2019
Accepted 9 November 2019
Available online 14 November 2019

Keywords:
Rare earth alloys and compounds
Electronic band structure
Superconductivity
Atomic disorder

ABSTRACT

The heat capacity, magnetic, and electrical transport properties of skutterudite-related $Y_5Rh_6Sn_{18}$ compound indicate intriguing coexistence of the high temperature thermal lattice relaxation process at temperatures higher than 350 K and superconductivity below the superconducting transition temperature $T_c = 3.08$ K. $Y_5Rh_6Sn_{18}$, having a cage-like structure crystallises in tetragonal structure with the space group $I4_1/acd$. The gap structure of this compound is found not to be characteristic of conventional BCS type superconductors. Anomalous behaviour observed in the electronic specific heat $C(T)/T$ and the upper critical field $H_{c2}(T)$ data may suggest the presence of two superconducting gaps in this compound. The *ab initio* band structure calculations showed a significant contribution of *s* and *p* Sn states as well as Rh and Y *d*-electron states to the total density of states near the Fermi level, which supports the multi-band superconductivity of this compound. Several electronic quantities and parameters characterising the superconducting and normal state of $Y_5Rh_6Sn_{18}$ are calculated within the Ginzburg-Landau-Abrikosov-Gorkov theory. The data reveals dirty limit superconductivity in $Y_5Rh_6Sn_{18}$ superconductor of type-II.

1. Introduction

The *f*-electron systems can be tuned through the magnetic quantum phase transition by applying the external pressure, magnetic field, or doping, at the border of magnetic order they often exhibit deviations from the thermodynamic and electric transport properties predicted by Landau Fermi-liquid theory. A wide variety of the strongly correlated electron phenomena found in this class of materials depend on ation between the rare-earth or actinide *f*-electron states and the conduction electron states, which defines either the Kondo (T_K) or indirect magnetic (T_{RKKY}) interactions. The subtle interplay between the both effects at the presence of crystal electric field can be a reason of new phenomena including small hybridisation gap semiconductivity [1], in which the hybridisation between the coherent *f* band and conduction electron bands can even induce the band inversion [2], valence fluctuation [3] and/or heavy fermion behaviour [4], non-Fermi liquid phase [5,6] and others [7]. The field skutterudite-related $Ce_3M_4Sn_{13}$ compounds, where *M* is a *d*-electron type metal, known as Remeika phases [8] have received renewed attention mainly because of the field-induced phase transition between the magnetically correlated heavy-fermion phase and a single-ion Kondo impurity state documented for the series, and accompanying quantum critical-like behaviours [9]. Among the family of these quasi-skutterudites all the *nonmagnetic* $La_3M_4Sn_{13}$ references have been reported as *s*-wave BCS superconductors with presence of atomic scale disorder leading to the appearance of *novel* superconducting state, characterised by the critical temperature $T_c^\star$ higher than T_c of the bulk phase [10,11]. This new phenomenon is a reason for continuing the study of atomic scale disorder and its impact on the superconductivity in strongly-correlated electron systems (SCES) [12,13], since the similar *high-temperature* inhomogeneous superconducting phase $T_c^\star$ with nano-scale disorder has also been reported for number of other SCES superconductors [14–18] and *high-T_c materials* [19,20].

The $LaM3_4Sn_{13}$ superconducting metals were examined in detail, leaving $Y_3Rh_4Sn_{13}$ as a possible candidate for study. However, reports about existence of $Y_3Rh_4Sn_{13}$ having exact stoichiometry are limited to only one report [21], while some superconducting properties of the Y–Rh–Sn system with stoichiometry similar to 3 : 4 : 13 were recently reported for $Y_5Rh_6Sn_{18}$ (symmetry $I4_1/acd$) in Refs. [22–24].

Crystal structure of rhodium based stannides is usually connected with a triple-perovskite-like cubic structure with stoichiometry $SnR_3Rh_4Sn_{12}$, which can accommodate multiple *R* cations

* Corresponding author. Institute of Physics, University of Silesia in Katowice, 75 Pułku Piechoty 1, 41-500, Chorzów, Poland.
E-mail address: andrzej.slebarski@us.edu.pl (A. Ślebarski).

https://doi.org/10.1016/j.jallcom.2019.152959
0925-8388/

like La, Ce, Pr, Nd, Sm, Gd, Eu, Yb, Ca, Sr, and Th [25]. The cubic symmetry does not support yttrium (atomic radius 180 p.m.) [26] as the R cation which is smaller than lanthanum (190 p.m.) and of the order of gadolinium (180 p.m.). However, the triple-perovskite stoichiometry can be realized for R = Y when much smaller germanium (125 p.m.) is used instead of tin (145 p.m.) [27]. In turn, for rhodium stannides with cations like Y or lanthanides smaller than Gd, like Er [28] a tetragonal lattice prevails (space group $I4_1/acd$) with overall stoichiometry $(Sn_{1-x}R_x)R_4Rh_6Sn_{18}$ (in the triple-perovskite convention it represents approximately a variation from $R_{3.33}Rh_4Sn_{12}$ to $R_{2.66}Rh_4Sn_{12.66}$) with continuous solid solution between the two extremes [29].

Despite its lack of stability we decided to investigate $Y_5Rh_6Sn_{18}$ as an equivalent of $Y_3Rh_4Sn_{13}$ system for several reasons. (*i*) It can possibly form a single phase with tin vacancies. (*ii*) Its superconductivity has not been known well so far. (*iii*) In the complex structure of $Y_5Rh_6Sn_{18}$ both, the atomic displacements as well as the nonstoichiometry of different crystallographic sites can be treated as structural defects (c.f. Refs. [11,30]), which could determine the superconducting properties of the system. (*iv*) Previous studies of $La_3Rh_4Sn_{13}$ (and similar isostructural compounds) revealed a structural second order-type transition at temperature $T^\star \sim 350$ K [11,31] due to displacive disorder [11] which converts the simple cubic high-temperature structure $Pm\bar{3}n$ into a body centred cubic structure $I4_132$ [32], as well as other distinct anomalies in the electrical resistivity at characteristic temperature $T_D \sim 160$ K $< T^\star$ with no structural signatures as a result of charge density wave (CDW) formation. We expected similar behaviour for $Y_5Rh_6Sn_{18}$. To better understand the nature of the T_D and $T^\star$ anomaly, we investigated magnetic susceptibility and resistivity as well as x-ray diffraction measurements were carried out, both in a wide temperature range up to 500 K.

2. Experimental and computational details

The $Y_3Rh_4Sn_{13}$-like sample was prepared by arc melting technique and then annealed at 870^{o}C for 2 weeks.

Electrical resistivity ρ at ambient pressure and magnetic fields was investigated by a conventional four-point ac technique using PPMS (physical properties measurement system) device.

Magnetic ac susceptibility was measured using the Quantum Design PPMS platform. The dc magnetic susceptibility and magnetisation were carried out in the temperature range 1.8− 400 K and in applied magnetic fields up to 7 T using a Quantum Design superconducting quantum interference device (SQUID) magnetometer.

The XPS spectra were obtained at room temperature using a PHI 5700 ESCA spectrometer with monochromatised Al K_α radiation.

The composition of Y−Rh−Sn system was studied using a JEOL JEM-3010 scanning electron microscope (SEM) equipped with an energy-dispersive spectrometry (EDS) microanalysis system. From the EDS analysis the average Y:Rh:Sn stoichiometric ratio obtained for 10 different regions of the sample surface was found to be 13.3± 0.7 : 18.7±0.3 : 60.0±0.7, which gives the formula unit $Y_{4.97}Rh_{6.0}Sn_{18.97}$ within the error 5.35, 1.86, and 0.98 atomic %, respectively for Y, Rh, or Sn elements, very similar to that, recently reported in Ref. [24]. For simplicity, this correct formula is replaced here by the expression $Y_5Rh_6Sn_{18}$.

The powder diffraction pattern of $Y_5Rh_6Sn_{18}$ was measured at the room temperature on PANalytical Empyrean diffractometer with the Cu Kα source. The compound was found to have a tetragonal structure with symmetry $I4_1/acd$. Powder synchrotron x-ray diffraction (XRD) studies have been carried out at the Swiss-Norwegian beamline (SNBL) at the European Synchrotron Radiation Facility (ESRF) in Grenoble, France. A temperature ramp between 200 K and 500 K was collected at BM1 beamline using Pylatus2M detector and $\lambda = 0.956906$ Å. The sample was loaded in a borosilicate capillary. The collection time was set to 10 s. For the high temperature range, the temperature was maintained using nitrogen blower (Cryostream800+) and each frame was collected with 10 s exposure and 100° sample rotation for a better powder average. Datafiles were processed using SNBL Bubble software suite [33] and the Rietveld refinement [34] was performed using Fullprof suite of programs [35]. The composition of the main phase refined at 200 K was found to be $Y_{5.1(3)}Rh_{6.0(3)}Sn_{17(1)}$, where the number in parentheses is a statistical uncertainty at 1-σ level. One can note that the stoichiometry of $Y_5Rh_6Sn_{18}$ shown by EDS method is slightly different than that, obtained from the powder diffraction pattern analysis. The reason for the observed discrepancy is that XRD sees only one phase of the sample, while EDS gives the result from the whole surface of the sample with various inhomogeneous regions. Therefore, the different stoichiometries are obtained depending on the method used (will be discussed in Sec. 3.3).

Theoretical study of the electronic structure we carried out for $Y_5Rh_6Sn_{18}$, using the WIEN2k package [36] which employees the DFT based full-potential linearised augmented plane waves (FP-LAPW) method complemented with local orbitals (LO) [37]. For the core states of constituent atoms the fully relativistic DFT approach was employed. For the set of local orbitals and valence states (assumed as follows: Y - $[4s^24p^6]_{LO}\{4d^15s^2\}_{VB}$; Rh - $[4s^24p^6]_{LO}\{4d^85s^1\}_{VB}$; Sn - $[4p^64d^{10}]_{LO}\{5s^25p^2\}_{VB}$) the scalar-relativistic Kohn-Sham was applied with spin-orbit coupling (SOC) accounted for by means of second variational method [37]. The generalised gradient approximation (GGA) form of the exchange-correlation energy functional was assumed, with parameterisation (PBEsol) derived for solids by Perdew *at al.* [38]. The band structure calculations were performed for the tetragonal system (space group $I4_1/acd$) with the chemical formula $(Sn_{1-x}Y_x)Y_4Rh_6Sn_{18}$, using the experimental lattice parameters and the positional parameters given in Table 1 (Choice 2 — BCT_2). During initial calculations the atomic position were relaxed to minimise interatomic forces. For all atoms the muffin-tin radii (R_{MT}) were used equal 0.127 nm. The values of parameters determining the accuracy of calculations were assumed as follows: $l_{max} = 10$, $G_{max} = 14$ and $K_{max} = 8.0/R_{MT} \simeq 0.175$ nm^{-1}. The k-mesh was tested against the total energy convergence and satisfactory precision, of few meV, was achieved with $7 \times 7 \times 7$ mesh ($N_k = 40\,\vec{k}$ vectors in irreducible Brillouine zone (*IBZ*)). Small dimensions of unit cell in reciprocal space can justify our choice for relatively small values of K_{max} and N_k parameters. It is worth note that despite the calculations were initialised from nonzero spin polarisation the convergence was reached at paramagnetic state.

3. Results and discussion

3.1. $Y_5Rh_6Sn_{18}$; structure, band structure, electrical transport properties and its thermodynamic characterisation in wide temperature range

The structure of $Y_5Rh_6Sn_{18}$ with space symmetry $I4_1/acd$ is more complex in reference to that of the cubic superconductor $La_3Rh_4Sn_{13}$ with symmetry $Pm\bar{3}n$, however, the band structures experimentally obtained for the both compounds are similar. Fig. 1 compares valence-band XPS spectra obtained at room temperature for $Y_5Rh_6Sn_{18}$ and $La_3Rh_4Sn_{13}$. Generally, the electronic valence bands of these two compounds are very similar, and dominated either by Rh 4*d* electron states, located in the XPS bands between the Fermi energy ε_F and ~ 5 eV, or by Sn 5*s* states with the broad maximum centred at ~ 7 eV, in agreement to DOS calculations for $Y_5Rh_6Sn_{18}$ and recent band structure calculations for $La_3Rh_4Sn_{13}$ [39], respectively. However, for $Y_5Rh_6Sn_{18}$ the XPS spectrum clearly shows the two-peak structure of the *d*-electron bands of Rh atoms,

Table 1
Positional parameters and the site symmetries in space group $I4_1/acd$ (No. 142) for $Y_5Rh_6Sn_{18}$ system. Lattice parameters (in Å) are: $a = 13.7532(1)$ and $c = 27.4686(4)$ at $T = 200$ K, and $a = 13.7985(2)$ and $c = 27.5584(5)$ at 500 K, respectively. Coordinates are listed in standard origin (choice 2) and origin (choice 1) used in Ref. [28] as well as in atom labelling scheme from entry 2106150 in COD [53], see text.

No.	Atom	Label			Wyckoff	Coordinates		Temperature	
	type	Ref. [28]	COD [53]	Text	site	Choice 1	Choice 2	200 K	500 K
1	Rh	$Rh_{(1)}$	Rh1	Rh1	16d	(0,0,z)	$(0,\frac{1}{4},z)$	$(0,\frac{1}{4},-0.0029(2))$	$(0,\frac{1}{4},-0.0029(3))$
2	Rh	$Rh_{(2)}$	Rh2	Rh2	32g	(x,y,z)	(x,y,z)	(0.2433(4),0.2515(4),-0.1227(3))	(0.2434(4),0.2515(4),-0.1229(3))
3	Y(Er)	Er(2)	Er1	Y2	32g	(x,y,z)	(x,y,z)	(0.1328(6),0.3860(6),-0.1923(3))	(0.1316(7),0.3851(7),-0.1915(3))
4	Y(Er)/Sn	Er(1)/Sn(1)	Er7/Sn7	Y1/Sn1	8b	$(0,0,\frac{1}{4})$	$(0,\frac{1}{4},\frac{1}{8})$	$(0,\frac{1}{4},\frac{1}{8})$	$(0,\frac{1}{4},\frac{1}{8})$
5	Sn	Sn(2)	Sn6	Sn2	32g	(x,y,z)	(x,y,z)	(0.0854(5),0.3395(5),-0.0811(2))	(0.0858(5),0.3395(5),-0.0812(2))
6	Sn	$Sn(3)_{(1)}$	Sn3	Sn3_1	16f	$(x,x,\frac{1}{4})$	$(x,x+\frac{1}{4},\frac{1}{8})$	$(0.1748(4),0.4248(4),\frac{1}{8})$	$(0.1742(4),0.4242(4),\frac{1}{8})$
7	Sn	$Sn(3)_{(2)}$	Sn2	Sn3_2	16f	$(x,x,\frac{1}{4})$	$(x,x+\frac{1}{4},\frac{1}{8})$	$(0.3246(4),0.5746(4),\frac{1}{8})$	$(0.3246(5),0.5746(5),\frac{1}{8})$
8	Sn	$Sn(3)_{(3)}$	Sn4	Sn3_3	32g	(x,y,z)	(x,y,z)	(0.3292(6),0.2617(4),-0.0382(3))	(0.3296(7),0.2625(4),-0.0382(3))
9	Sn	$Sn(3)_{(4)}$	Sn5	Sn3_4	32g	(x,y,z)	(x,y,z)	(0.0016(3),0.5753(5),-0.0365(3))	(0.0003(4),0.5755(6),-0.0363(3))
10	Sn	$Sn_{(4)}$	Sn1	Sn4	16e	$(\frac{1}{4},y,\frac{1}{8})$	$(\frac{1}{4},x,0)$	$(\frac{1}{4},0.4780(12),0)$	$(\frac{1}{4},0.4791(12),0)$

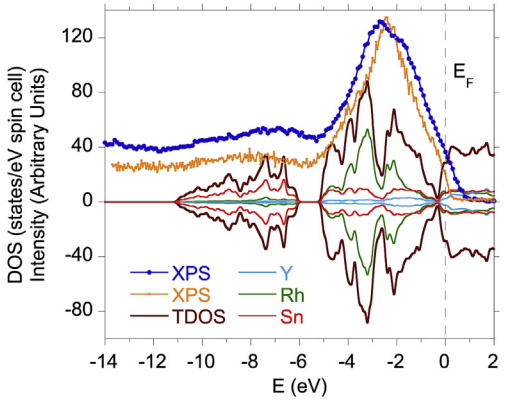

Fig. 1. Valence band XPS spectra for $Y_5Rh_6Sn_{18}$ (blue points) are compared with the calculated total density of states within the LSDA approximation (brown line). For comparison, the figure also shows the VB XPS spectra for $La_3Rh_4Sn_{13}$ (yellow points). The blue, green and red lines represent the atomic DOSs calculated for Y, Rh, and Sn, respectively in the (eV spin cell)$^{-1}$ units. (For interpretation of the references to colour in this figure legend, the reader is referred to the Web version of this article.)

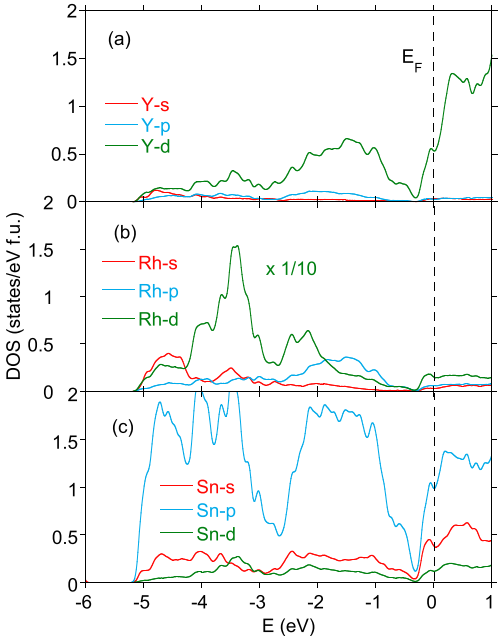

Fig. 2. Sum of the *s*, *p*, and *d* electronic states in respective valence bands of Y, Rh, and Sn in the $Y_5Rh_6Sn_{18}$ formula unit (atomic positions are listed in Table 1), located near the Fermi level. In panel (*b*) sum of the *d*-electron states for four Rh atoms is multiplied by 1/10 to present all remaining atomic DOSs in the same scale.

which is poorly visible, but noticeable for $La_3Rh_4Sn_{13}$. We have previously documented that such a more complex structure of Rh bands in the VB XPS spectra can be observed for the skutterudite-related 3 : 4 : 13-like systems with a larger atomic disorder [11], which is a cause of appearance of their superstructure with larger cell volume.

The *bare* Sommerfeld coefficient calculated for the DOS at the Fermi level amounts to 16.8 mJ/mol K^2 for $Y_5Rh_6Sn_{18}$ (for comparison, the *bare* γ coefficient calculated from the DOS at ε_F is 13 mJ/mol K^2 for $La_3Rh_4Sn_{13}$. For the both compounds this value is in good agreement with that estimated from the low-temperature specific heat measurements (will be discussed). $Y_5Rh_6Sn_{18}$ is calculated paramagnetic (i.e., with non-spin polarised solution and calculated total magnetic moment as well as magnetic moments of various Ce, Rh, and Sn atoms equal zero). We started to calculate the DOSs for ferromagnetic system, however, the calculations predicted the paramagnetic ground state of $Y_5Rh_6Sn_{18}$. The electronic states located at the Fermi level are mostly of *s* (Sn), *p* (Sn), and *d* (Y, Rh) orbital symmetry. Fig. 2 shows the energy distribution of the summarised states *s*, *p*, and *d* for all Y, Rh and Sn atoms in the $Y_5Rh_6Sn_{18}$ formula unit, respectively located near the Fermi energy.

In our recent report [40] we documented for the series of $Ce_3M_4Sn_{13}$ and $La_3M_4Sn_{13}$ isostructural compounds that the asymmetry of the Sn 4*d* XPS spectra can be associate with the change of local symmetry of the $Sn1(Sn2)_{12}$ cages due to strong covalent bonding between the atoms Sn1 and Sn2. We therefore suspect similar line-shape effect for cage-like $Y_5Rh_6Sn_{18}$. Fig. 3 compares the Sn 4*d* XPS spectra obtained for $Y_5Rh_6Sn_{18}$ and $La_3Rh_4Sn_{13}$. The asymmetry of the both lines is qualitatively similar, however, more pronounced effect is visible for $Y_5Rh_6Sn_{18}$, which suggests its stronger covalent bondings and/or the presence of other electronic states on the higher energy side of the spectrum. Indeed, the calculations (in Fig. 3*b*) showed the complex structure of various Sn 4*d* states, as well as the presence of the Y 4*p* states in this spectrum.

The bulk nature of superconductivity in $Y_5Rh_6Sn_{18}$ was established by magnetic susceptibility $\chi(T)$, as shown in Figs. 4 and 5. The χ versus T dc magnetic susceptibility measured at 500 Oe in zero field (ZFC) and field cooling (FC) modes exhibits bifurcation in ZFC and FC data below $\sim$ 350 K (Fig. 4), similar to that, reported for $La_3Rh_4Sn_{13}$ [11,31], while in the superconducting state ($T < T_c \cong 3.1$ K) it reveals the onset of diamagnetism associated with the

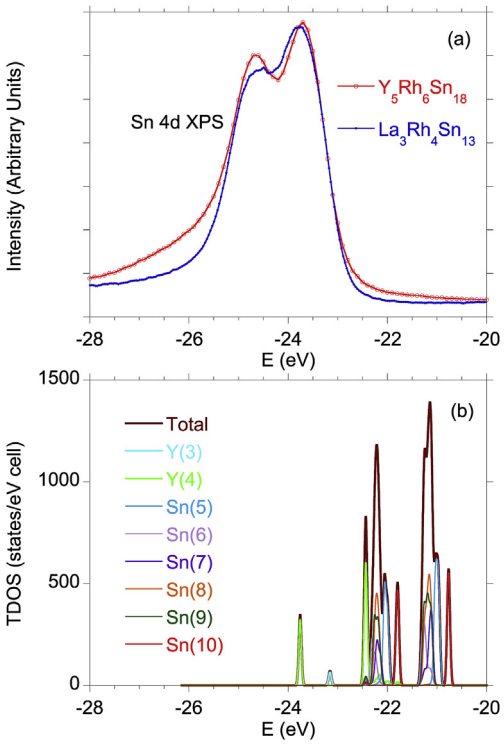

Fig. 3. The Sn 4*d* XPS spectra for $Y_5Rh_6Sn_{18}$ are compared to the similar spectra of $La_3Rh_4Sn_{13}$ [in panel (*a*)]. Panel (*b*) presents total 4*d*-electron Sn-DOSs and Y 4*p* DOSs calculated for different atoms listed in Table 1.

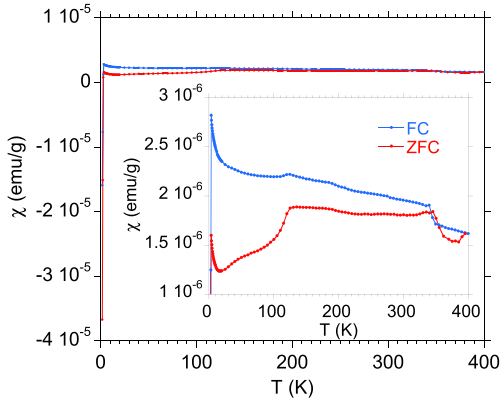

Fig. 4. Magnetic susceptibility (dc) for $Y_5Rh_6Sn_{18}$ in a field-cooled (FC) and zero-field-cooled (ZFC) experiment with an applied field 0.05 T.

superconductivity. The sharp drop below 120 K shown in $\chi_{dc}(T)$ data well correlates with an anomalous change in the specific heat $C(T)$ and can be related to appearance of the CDW phase (will be discussed), while its small rice below 20 K shown in Fig. 4 can be addressed to presence of paramagnetic impurities and/or structural defects (c.f. similar low-temperature rice was observed and discussed for *nonmagnetic* $Ca_3Rh_4Sn_{13}$ [11]).

Similarly, the ac susceptibility (Fig. 5) displays a robust diamagnetic signal due to superconducting transition at T_c. The perfect diamagnetism of the full Meissner state with $\chi' = -1/(4\pi d) = 9.8 \times 10^{-3}$ emu/g for mass density $d = 8.14$ g/cm^3 is reached for $Y_5Rh_6Sn_{18}$ below 2.6 K. Imaginary (χ'') part of ac mass magnetic susceptibility χ_{ac} shows the maximum at $T_{max} = 2.86$ K, which well characterises the full Meissner state of the sample. The $\chi'(T)$ component also demonstrates for $Y_5Rh_6Sn_{18}$ an anomalous

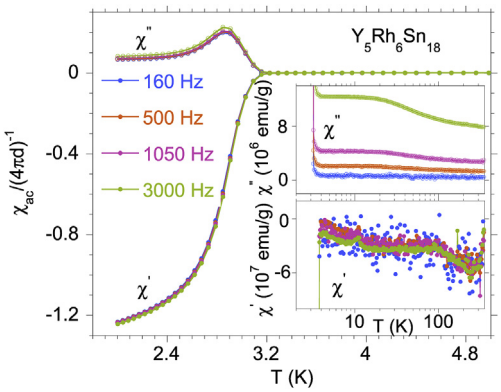

Fig. 5. The real and imaginary components of the ac magnetic susceptibility χ_{ac} (χ' and χ'') for $Y_5Rh_6Sn_{18}$, as a function of temperature measured at different frequencies in a field $B = 2$ Oe. The main panel shows the superconductivity volume fraction, i.e., $\chi_{ac}/(4\pi d)^{-1}$. The bare value of $\left|\chi_{ac}/(4\pi d)^{-1}\right| > 1$ is due to the diamagnetic character of the sample at $T > T_c$.

behaviour at ~ 120 K and ~ 300 K, and its low-T frequency dependent rise, which indicates the presence of structural defects.

Fig. 6 shows temperature dependence of electrical resistivity $\rho(T)$ for $Y_5Rh_6Sn_{18}$ in various magnetic fields. The critical temperature T_c is defined as the temperature at which ρ falls to 50% of its normal state value. In the temperature range $T_c < T \lesssim 100$ K resistivity exhibits a positive magnetoresistivity $MR = [\rho(B) - \rho(0)]/\rho(0)$ with the maximum value of $MR \sim 9\%$ at T_c for applied fields $B < 5$ T. The similar positive MR effect is characteristic of the family of skutterudite-related compounds $Ce_3M_4Sn_{13}$ and $La_3M_4Sn_{13}$ [13] and results from *d*-electron correlations in these materials. Fig. 7 displays the cooling-heating and field evolution of $\rho(T)$ data in the temperature range $250 < T < 320$ K. A clear hump-like feature emerges in the first cooling run, while for next heating run it disappears. We noted that intensity of this hump-like feature and its thermal hysteresis ΔT is reduced in the next cooling/heating cycles. The cooling run hump-like feature is also reduced by magnetic field, as is shown in the inset to Fig. 7. After more than four cycles the remaining weak hump-like feature is still present in $\rho(T)$ data between ~ 250 and 320 K, however, it does not depend on further thermal treatment. The high temperature resistivity hump-like feature roughly correlates with the abnormal behaviour in the χ_{dc} and χ' data at about ~ 300 K (see Figs. 4 and 5) and specific heat anomalies shown in Fig. 8. The phenomenon seen in the electrical resistivity is most likely related to the process of thermal lattice relaxation. In order to explain the nature of this anomaly we

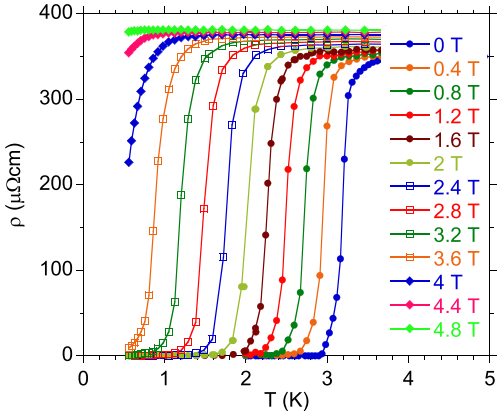

Fig. 6. Electrical resistivity at various applied magnetic field for superconducting phase of $Y_5Rh_6Sn_{18}$.

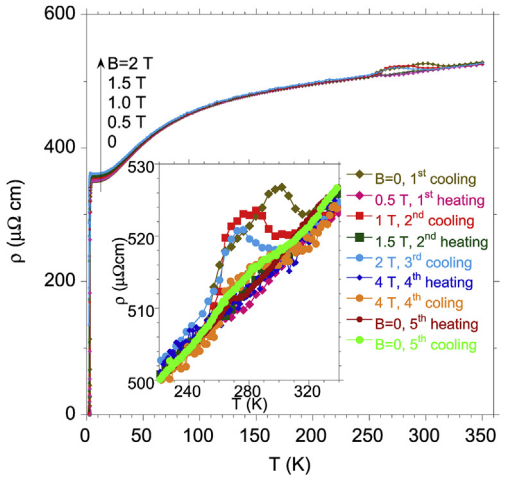

Fig. 7. Electrical resistivity in cooling/heating cycles for $Y_5Rh_6Sn_{18}$.

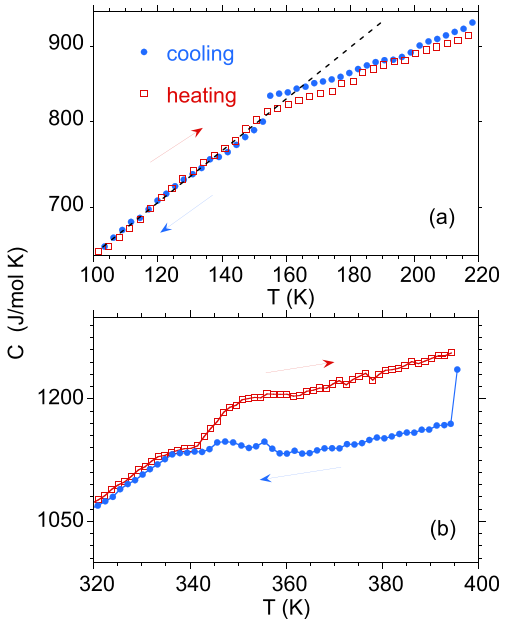

Fig. 8. High temperature specific-heat $C(T)$ for $Y_5Rh_6Sn_{18}$ measured first in the heating (red squares) and then in cooling (blue points) process in the temperature region between 0.4 K and 390 K. Panel (a) displays the $C(T)$ data with a clear kink in $C(T)$ different slopes above and below $T = 155$ K. Panel (b) shows abnormal behaviour with thermal hysteresis at temperatures $T > 343$ K. The effect of the both anomalies in high-T $C(T)$ data is reproducible in several measurements. (For interpretation of the references to colour in this figure legend, the reader is referred to the Web version of this article.)

performed synchrotron XRD at wide temperature range above and below the ρ hump.

Fig. 9 displays the magnetisation M versus magnetic field B isotherms for $Y_5Rh_6Sn_{18}$ with hysteresis loops for $T < T_c$ due to vortex pinning effect, and the diamagnetic $M(B)$ behaviour related to Rh atoms.

In the inset we show the hysteresis loop of $\Delta M(B)$ at $T = 2$ K that is defined by $M(B)$ at 2 K minus a diamagnetic background $\chi_d B$ with $\chi_d = -8.88 \times 10^{-7}$ emu/g Oe. A hysteresis loop suggests a type-II superconductor with a critical field $H_{c1} < 80$ Gs. The expected [41] $H_{c1}(0) = H_c(0) \ln \kappa(\sqrt{2}\kappa)^{-1} = 3.5$ Gs for estimate of the thermodynamic critical field $H_{c0}(0) = \left(\frac{3\gamma_0}{2\pi^2 k_B^2}\right)^{1/2} \Delta_c(0) \cong 85$ Gs [$\gamma_0 = 813.8$

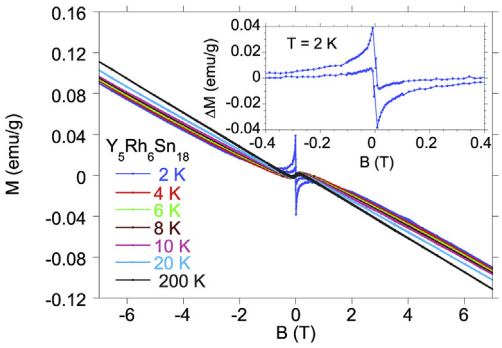

Fig. 9. Magnetisation M vs magnetic field B for $Y_5Rh_6Sn_{18}$ at different temperatures. The inset exhibits hysteresis loop for superconducting state. $\Delta M_{2K}(B)$ is the magnetisation isotherm $M_{2K}(B)$ subtracted by background $\chi_d \times B$, for $\chi_d = -8.88 \times 10^{-7}$ emu/(g Oe). At $T > T_c$ the $M(B)$ isotherms exhibit diamagnetism of the sample.

erg/cm^3 K^2, $\kappa_{GL} \sim 74$ (cf. Sec. 3.2)], alternatively $H_{c1}(0)$ is ~ 15 Gs using the formula $H_c(0) = 4.23\sqrt{\gamma_0} T_c(1-t) \cong 371$ Gs in the limit $t = T/T_c \to 0$.

Shown in Fig. 10 is the specific heat plotted as $C(T)/T$ at various magnetic fields. The heat capacity data indicate bulk superconductivity below $T_c = 3.08$ K, slightly smaller than $T_c^{\star} = 3.20$ K obtained from electrical resistivity. The $C(T)/T$ data can be approximated by the expression $C(T)/T = \gamma + \beta T^2 + \frac{1}{T} A \exp[-\Delta_c(0)/k_B T]$. The best fit gives an electronic coefficient $\gamma = 15.3 \pm 1.1$ mJ/mol K^2, $\beta = 7 \pm 0.9$ mJ/mol K^4 and the energy gap at $T = 0$,

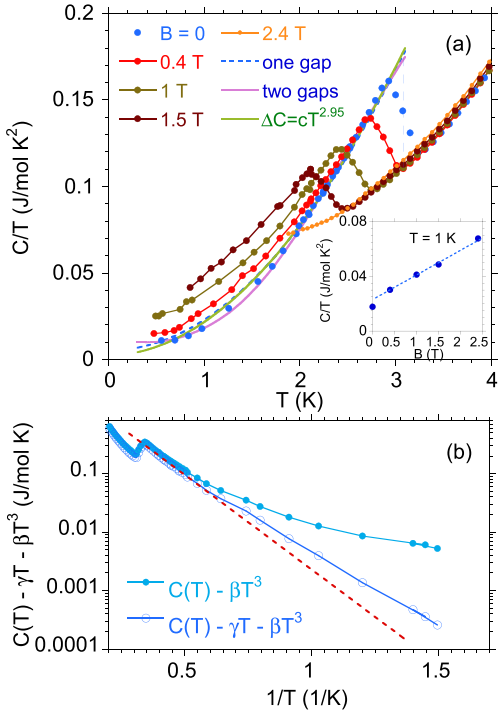

Fig. 10. (a) Temperature dependence of specific heat, $C(T)/T$, for $Y_5Rh_6Sn_{18}$ in various magnetic fields. The dotted blue line is the best fit of the expression $C(T)/T = \gamma + \beta T^2 + \frac{1}{T} A \exp(-\Delta_c(0)/k_B T)$ to the data ($Chisq = 2.6 \times 10^{-4}$). The solid violet line is a fit of two-gap model to the $C(T)/T$ at $B = 0$, considering the phonon ($C_{ph} = \beta' T^3$) and electronic ($\gamma' T$) contributions (Eq. (5), $Chisq = 8.3 \times 10^{-5}$). The solid green line shows the power law approximation of the expression $C(T)/T = \gamma'' + \beta'' T^2 + cT^{\alpha'}$, $\alpha' = 1.95$, and $\Delta C = cT^{2.95}$ ($Chisq = 2.3 \times 10^{-4}$). The inset exhibits C/T at 1 K vs. magnetic field B. The parameters γ and β are obtained similar from all different approximations. Panel (b) shows specific heat $C(T, B = 0) - \gamma' T - \beta' T^3$ in a log scale vs. the inverse temperature, $1/T$. (For interpretation of the references to colour in this figure legend, the reader is referred to the Web version of this article.)

$\Delta_c(0)/k_B = 7.6\pm0.11$ K. For $N = 29$ atoms in formula unit, $\beta = N(12/5)\pi^4 R\theta_D^{-3}$ gives the Debye temperature, $\theta_D \sim 200.4\pm$ 10 K. We estimated $\Delta C/(\gamma_0 T_c) \cong 2.0(5)$. We also determined $2\Delta_c(0)/k_B T_c \approx 4.92$ which is larger than that expected from the BCS theory ($2\Delta_c(0)/k_B T_c = 3.52$). The $C/T \sim \exp[-\Delta_c(0)/k_B T]$ exponential behaviour and the proper calculated quantities obtained from the specific heat data indicate that $Y_5Rh_6Sn_{18}$ may be categorised as a strong coupling *s*-wave BCS superconductor. Following by Bhattaacharyya et al. [24] the $\Delta C(T) = C(T) - \gamma'' T - \beta'' T^3$ can also be approximated by a power law $\Delta C(T) = cT^{\alpha}$ with an exponent $\alpha = 2.95$, which suggests that $Y_5Rh_6Sn_{18}$ has an anisotropic superconducting gap. It should be noted, however, that the best fit to the $C(T)$ data in the temperature range $T < T_c$ gives the multi-band model (details in Fig. 10).

Within the Eliashberg theory of strong-coupling superconductivity [42], the McMillan expression [43,44],

$$T_c = \frac{\theta_D}{1.45}\exp\left\{\frac{-1.04(1+\lambda)}{\lambda - \mu^*(1+0.62\lambda)}\right\}, \quad (1)$$

gives an estimate of the electron-phonon coupling parameter $\lambda \approx 0.54$ (for $T_c^{\star}$ phase $\lambda^{\star} \approx 0.55$), when the Coulomb repulsion $\mu^{\star}$ is assumed to be ~ 0.1 as a typical value known for *s* and *p* band superconductors [43,45]. A similar λ was estimated for $La_3Rh_4Sn_{13}$ superconductor [10]. From free electron theory, the normal state electronic specific heat coefficient $\gamma_0 \equiv C(T)/T$ is related to the bare density of states at the Fermi level $N(\varepsilon_F)$ by equation

$$\gamma_0 = \frac{\pi^2 k_B^2 N_A}{3} N(\varepsilon_F)(1+\lambda). \quad (2)$$

The DOS at ε_F is $N(\varepsilon_F) = 9.64$ states/eV f.u. or 9.58 states/eV f.u., respectively for λ or $\lambda^{\star}$, based on a value of the electronic specific heat coefficient $\gamma_0^{exp} = 39$ mJ/mol K^2 obtained in the superconducting state $T \le T_c$ from the linear dependence of C/T against T^2 at $T = 0$ and at magnetic field of 2.4 T. The coefficient γ_0^{exp} compares well with the $\gamma_0^{calc} \times (1+\lambda) = 25.9$ mJ/mol K^2 for $N(E_F) = 7.13$ states/eV f.u. from *ab initio* calculations.

Fig. 11 displays the $H - T$ phase diagram. The critical temperatures were determined from resistivity ($T_c^{\star}$, blue points) or from the specific heat data (T_c phase, red squares), respectively.

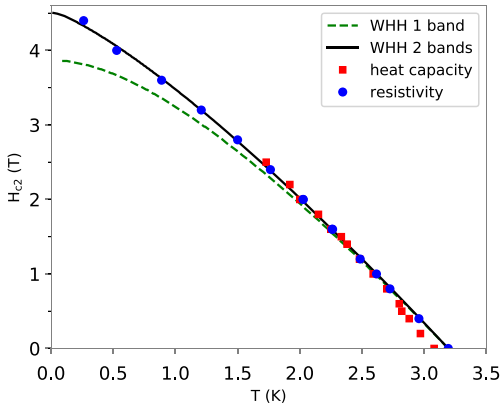

Fig. 11. Temperature dependence of the upper critical field H_{c2} in the $H-T$ phase diagram for $Y_5Rh_6Sn_{18}$. The blue points show T_c values obtained from electrical resistivity data under H, and defined as the temperature at which ρ drops to 50% of its normal-state value. The red squares represent T_c obtained from $C(T)/T$ vs T data in Fig. 10. The dashed green (solid black) line represents results from the Werthamer–Helfand–Hohenberg a one–band (two–band) dirty type–II superconductor. (For interpretation of the references to colour in this figure legend, the reader is referred to the Web version of this article.)

Our previous studies of the series of $La_3M_4Sn_{13}$ superconductors have documented that the separation of the $T_c^{\star}$ and T_c superconducting phases was enhanced by an increase of atomic disorder [10,46], the largest one was obtained for $La_3Ru_4Sn_{13}$. Shown in Fig. 11 the $H - T$ phase diagram is very similar to that of $La_3Rh_4Sn_{13}$. The maximum difference $\Delta T_c = T_c^{\star} - T_c \sim 0.15$ K occurs for $H = 0$, with increasing of H ΔT_c decreases, while for $H > 1$ T the difference between the *high temperature* inhomogeneous superconducting state $T_c^{\star}$ and the *bulk* superconducting phase T_c is no longer visible. The $H - T$ data near T_c are not enough well approximated by the Ginzburg–Landau (GL) theory. The best fit of equation $H_{c2}(T) = H_{c2}(0)\frac{1-t^2}{1+t^2}$ gives the upper critical field values of $H_{c2}(0) \approx 4.3$ T and $T_c^{GL} = 3.29$ K, larger than T_c and $T_c^{\star}$. From the Ginzburg–Landau relation [47] $\mu_0 H_{c2}(0) = \Phi_0/2\pi\xi_{GL}(0)^2$ we estimated the superconducting coherence length $\xi_{GL}(0) = 9$ nm, where $\Phi_0 = h/2e = 2.068 \times 10^{-15}$ T m^2 is the flux quantum.

3.2. Superconductivity of $Y_5Rh_6Sn_{18}$ in the presence of atomic disorder; superconductivity modelling

From the microscopic point of view the temperature dependence of H_{c2} in dirty superconductors, i.e., superconductors where the coherence length ξ is larger than the mean free path, is normally explained with the Werthamer–Helfand–Hohenberg (WHH) [48,49] or Maki–de Gennes [50] theories. They take into account the orbital and paramagnetic effects of an external fields as well as nonmagnetic and spin-orbit scattering. The WHH theory predicts a linear temperature dependence of H_{c2} near T_c, what agrees with the data presented in Fig. 11. However, it also predicts that in the dirty limit

$$H_{c2}(0) = -0.69 T_c \left.\frac{dH_{c2}}{dT}\right|_{T=T_c}, \quad (3)$$

which gives $H_{c2}(0) = 3.86$ T, whereas the actual value is around 4.7 T. The temperature dependence of H_{c2} from WHH theory is shown as the dashed green line in Fig. 11. It is obvious from this figure that WHH theory underestimates the upper critical field at low temperatures by predicting much larger curvature of $H_{c2}(T)$. We estimate the mean free path $l \approx 6.2$ nm (see later) what, when compared to $\xi \approx 9$ nm does not locate our system deeply in the dirty limit. However, in the clean limit the coefficient in Eq. (3) is 0.73 instead of 0.69 [49], which is still too small to explain the measured value of $H_{c2}(0)$.

The deviation from the WHH curve can have different sources. For example, strong–coupling effects can yield an enhancements of $H_{c2}(0)$ and we estimated $2\Delta_c(0)/k_B T_c \approx 4.92$. This effect, however, is reduced in the case of disordered superconductors [51]. Other possible explanations include, e.g., the spin–orbit coupling, Fermi–surface anisotropy or granularity. The results presented in Sec. 3.1 can suggest that for the present system $H_{c2}(T)$ can also be affected by the presence of two bands. In this case the critical field can be calculated from the theory of Gurevich [52], which is obtained by adapting the Eilenberger and Usadel equations to the case of a two–band dirty superconductor.

$$a_0[\ln t + U(h)] \times [\ln t + U(\eta h)] + a_2[\ln t + U(\eta h)] + a_1[\ln t + U(h)] = 0, \quad (4)$$

where $U(x) \equiv \psi(x + 1/2) - \psi(1/2)$, $\psi(\ldots)$ is the di–gamma function, $t = T/T_c$, h is reduced magnetic field defined as $h = H_{c2}D_1/2\Phi_0 T$, D_1 is the band diffusivity, $\eta = D_2/D_1$. The parameters $a_{0,1,2}$ can be expressed by the intra– and interband BCS superconducting coupling constants λ_{11}, λ_{22}, λ_{12} and λ_{21}. We are aware that though the agreement between the experimental data and theoretical approximation is satisfactory, there remains questionable

reliability of obtaining parameters since the fit was done for a number of fitting parameters. Nonetheless, the *ab initio* band structure calculations, that showed a significant impact of *s* and *p* Sn bands as well as Rh and Y *d*-electron states at the Fermi level of $Y_5Rh_6Sn_{18}$ (see Fig. 2) are a strong support for the two-band scenario. The electronic specific heat shown in Fig. 10*a* can also be the reasonable confirmation of the two(multi)-gaps model. In the one-gap BCS description, one expects the linear plot of the electronic specific heat $C(T) - \gamma_0 T - \beta T^3 = A \exp[-\Delta_c(0)/k_B T]$ in a log scale vs. the inverse of temperature, $1/T$ (see Fig. 10*b*). This is, however, not a case. A straight line cannot be used to describe the data at the lowest temperatures between 0.4 and 2 K, this observation allows us to propose that the superconductivity in $Y_5Rh_6Sn_{18}$ is not a classic isotropic s-wave BCS-type. Alternatively, the electronic specific heat $C(T)/T$ data of the $Y_5Rh_6Sn_{18}$ superconductor are well fitted using two-gap model (Eq. (5)):

$$\frac{C(T)}{T} = \gamma' + \beta' T^2 + \frac{1}{T} A \left[\eta \exp\left(-\frac{\Delta_1}{k_B T} \right) + (1-\eta) \exp\left(-\frac{\Delta_2}{k_B T} \right) \right]. \quad (5)$$

In the two-gap scenario, electronic specific heat is assumed to be the sum of two contributions with different values of superconducting gaps Δ_1 and Δ_2. The result of the best fit with Eq. (5) for the parameters $\Delta_1/k_B = 8.7 \pm 1.0$ K, $\Delta_2/k_B = 3.9 \pm 1.9$ K, $\eta = 0.96 \pm 0.04$, $\gamma' = 12.8 \pm 2$ mJ/mol K^2, and $\beta' = 6.5 \pm 1$ mJ/mol K^4 is illustrated by the solid violet curve in Fig. 10. The electronic specific heat coefficient γ' and coefficient β' in phonon contribution are similar to that, obtained from the approximation with the use of simple *s*-wave model.

The two-band dirty superconductor model gives the extrapolated zero-temperature upper critical field $H_{c2}(0) = 4.7$ T corresponding to $\xi_{GL}(0) = 8.4$ nm, which seems to be reasonable since $\xi_{GL} > l$ (l is an electric transport scattering length) has the same order of magnitude as that, estimated from relation [41]; $\xi^d_{GL}(0) = \frac{8.57 \times 10^{-7}}{(\gamma_0 \rho_n T_c)^{1/2}(1-t)^{1/2}} \approx 9.2$ nm ($\rho_n = 350 \times 10^{-6}$ Ωcm is a normal state resistivity approximated to $T = 0$, $\gamma_0 = 813.8$ erg/cm^3 K^2, and $t \to 0$). In the frame of Ginzburg-Landau-Abrikosov-Gorkov (GLAG) theory of the type-II superconductors [48] the slope of $\frac{dH_{c2}}{dT}$ at T_c is [41]:

$$-\left.\frac{dH_{c2}}{dT}\right|_{T=T_c} = \left[9.55 \times 10^{24} \gamma_0^2 T_c \left(n^{2/3} \frac{S}{S_F} \right)^{-2} + 5.26 \times 10^4 \gamma_0 \rho_n \right] [R(\lambda_{tr})]^{-1} \quad (6)$$

in units Gs/K, where n is the density of conduction electrons in cm^{-3}, S/S_F is the ratio of the Fermi surface area to the Fermi surface of the free electron gas, $S_F = 4\pi(3\pi^2 n)^{2/3}$, and $R(\lambda_{tr})$ is the Gorkov function of order unity ($R(0) = 1$, $R(\infty) = 1.17$ [41]). For $\left(\frac{dH_{c2}}{dT}\right)_{T_c} = -2.07 \times 10^4$ Gs/K (in Fig. 11) we have calculated the value $n^{2/3} S/S_F = 5.83 \times 10^{13}$ cm^2, taking $R(\lambda_{tr}) = 1$, when $\lambda_{tr} = 5.51 \times 10^{-21} \rho_n (n^{2/3} S/S_F)(\gamma_0 T_c)^{-1}$ is calculated 4.4×10^{-14} for $Y_5Rh_6Sn_{18}$. Then, the electronic mean free path $l(0) = 1.27 \times 10^4 [\rho_n (n^{2/3} S/S_F)]^{-1} = 6.2$ nm is obtained smaller than the coherence length ξ_{GL}.

In a dirty limit, the Ginzburg-Landau penetration depth $\lambda^d_{GL} = 6.42 \times 10^{-3} (\rho_n/T_c)^{1/2} (1-t)^{-1/2} = 682$ nm gives GLAG parameter $\kappa = \lambda^d_{GL}(0)/\xi_{GL}(0) = 74.2$, in agreement with alternative estimate of $\kappa^d_{GL} \approx 74.8$ on the base of expression $\kappa^d_{GL} = 7.49 \times 10^3 \gamma_0^{1/2} \rho_n$ defined in Ref. [41]. The large $\kappa^d_{GL} \gg 1$ value establishes $Y_5Rh_6Sn_{18}$ to be a superconductor of type II.

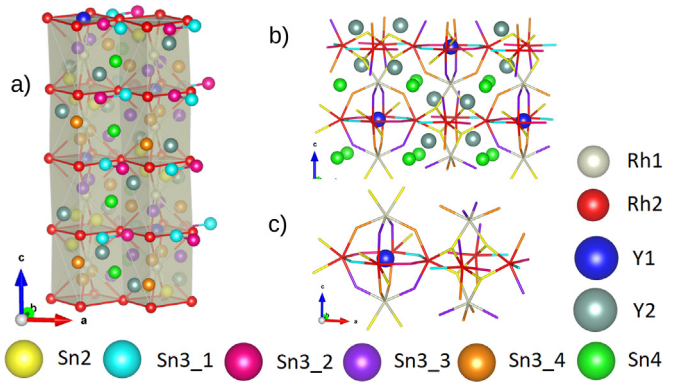

Fig. 12. Schematic view of the crystal structure, which can be represented as Rh-based almost square prisms ($a \approx 5.0$ Å, $c \approx 6.8$ Å) extending along the c-axis with channels filled with dumbbells of Sn3_1 and Sn3_2 as well as Sn4 atoms (a). A connectivity is provided by bonds ≈2.8 Å(b). Y1 atom is coordinated by a cage of Sn3_(1,2,3,4), Rh1 and Rh2 (c). The linkage (<2.8 Å) along the ab-plane is provided through Sn3_(1,2,3,4)-Rh2-Sn2 contacts and along the c-axis by Sn3_3/Sn3_4-Rh1-Sn2-Rh2 (c). Y2 and Sn4 atoms are omitted in panel (c).

3.3. Insight into structural properties of $Y_5Rh_6Sn_{18-x}$–type structure at high temperature limit

The crystal structure has been modelled in a tetragonal $I4_1/acd$ space group (No. 142), which has been proposed by Hodeau *et al.* [28] and is deposited in the Crystallography Open Database (COD) [53] as entry No. 2106150. The space group has two alternative origin choices. In this paper a standard origin choice 2 is used, while the paper [28] and the COD used the origin choice 1. Additionally, the other authors also used a different naming scheme, which might cause confusion. Table 1 contains mapping between coordinates in standard origin (choice 2) and origin choice 1 used in Ref. [28] as well as atom labelling scheme from entry 2106150 in the COD [53]. The unit cell contains 10 crystallographically independent sites and its large dimensions make it difficult to visualise in a simple fashion. In this paper we would like to present an alternative way to look at this type of structure, which emphasises a tetragonal layered-perovskite-like character of the lattice and not a pseudocubic coordination of Sn. In this context the framework is based on corrugated rhodium (Rh2) planes (Fig. 12a) and Rh1 square prisms, which are coupled by tin along the ab-plane and the c-axis (Fig. 12b). In particular, the a/b-axis connectivity is provided by bonds of about 2.8 Å between Sn3_(1,2,3,4)-Rh2-Sn2 and along the c-axis by Sn3_3/Sn3_4-Rh1-Sn2-Rh2 (Fig. 12c). The Y1 acts either as a centre for the Rh2 square (d ≈3.5 Å) and its fixed position does not allow to move inside the cage (Fig. 12c). On the other hand Y2 is in the second shell (d ≈3.1 Å) of both Rh1 and Rh2, therefore it also might take part in electron transfer. Sn4 is far (3–5 Å) away from most atoms, which makes it weakly coupled to the lattice. A special comment must be made about Sn2 site, which

has multiple roles. First, it belongs to close contact pathways both along the ab-plane and the c-axis (right hand of Fig. 12c), which potentially makes it sensitive to changes in both crystallographic directions. At the same time, it forms a tetrahedron (d = 3.41 Å), which plays a role equivalent to the Y1 site in centring of the Rh1-prism. The tetragonal arrangement makes Sn2 closely packed to each other, which hinders their free movement despite fully refineable atomic coordinates.

The Rietveld [34] refinement performed on datasets collected between 200 K and 500 K allowed to connect variations observed in resistance (inset to Fig. 7) and specific heat (Fig. 8b) with changes in the crystal structure. The first observation was connected with subtle variations of the unit cell volume (Fig. 13). In order to visualise the changes a straight line (black) was fit to the volume (red dots) in the whole temperature range and then subtracted from it (blue dots). The observed deviations from the linear trend are of the order of 0.5 $Å^3$ but much bigger than uncertainty of the fit 0.1 $Å^3$ (blue bars). Two distinct inflection points can be observed: one around 300 K where the curve has a clear minimum and the second one around 355 K where the curve regains a linear trend. The lower temperature corresponds well with the observed history effect in the resistance curve (Fig. 7), while the higher one with the abnormal behaviour of the specific heat (Fig. 8b). It must be noted that the refinement of the cell volume (peak positions) is almost completely uncorrelated with the atomic coordinates (peak intensities), so it does not directly depend on the unit cell contents. At the second stage the data was examined with respect to a possible superstructure or a short range order similar to the one observed in $La_3Rh_4Sn_{13}$ [11]. No indication of any of the above effects was found in the data and an example of temperature dependence of a selected angular range in presented Fig. 14.

The next step comprised refinement of atomic coordinates, atomic displacement parameters (ADPs) and site occupancies. For all plots check Appendix A. Similarly to Hodeau *et al.* [28] a possible Sn1/Y1 Table 1 site disorder was expected, which was included in the refinement as a variable Sn/Y ratio with a total occupancy constrained to 1. The refinement of the ratio resulted in a clear preference for yttrium −0.10(4)/1.10(4) and no tin, therefore only Y1 was kept and refined for all temperatures (the negative quantity of tin indicated that even with the lighter Y, the site might not be fully occupied). Then the occupancies of remaining sites (Rh1 was fixed to 1.0) were refined and at 300 K they were equal to: Rh1 1.0(fix), Rh2 0.88(7), Y1 0.80(4), Y2 0.97(5), Sn2 0.80(4), Sn3_1 0.83(5), Sn3_2 0.90(6), Sn3_3 0.79(5), Sn3_4 0.96(6), Sn4 0.96(5), which gave the

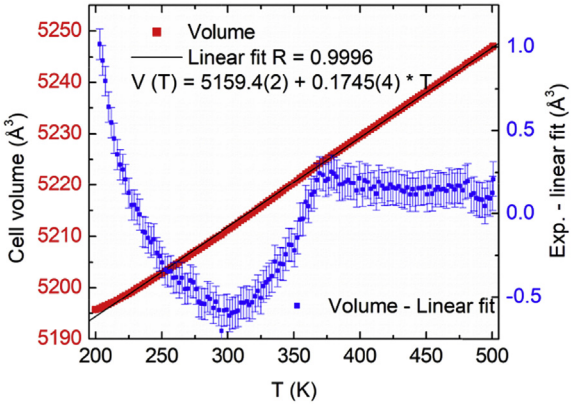

Fig. 13. Temperature dependence of the unit cell volume (red, left axis). In order to enhance subtle changes a straight line was fit (black) and subtracted from the data (blue, right axis). Clear changes in slope are observed at 300 K and 355 K after which a linear trend is recovered. (For interpretation of the references to colour in this figure legend, the reader is referred to the Web version of this article.)

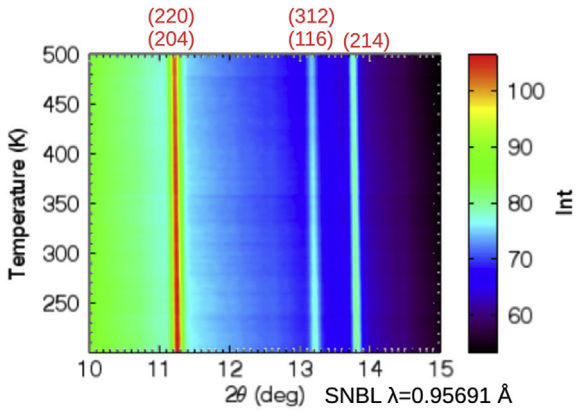

Fig. 14. Temperature dependence of the low part of the diffraction patterns did not reveal any superstructure peaks or sudden changes in background. The refinement was performed using the same structural model for all temperatures.

total stoichiometry of $Y_{5.1(3)}Rh_{6.0(3)}Sn_{17(1)}$. The numbers in parentheses represent a statistical uncertainty on each site, which results in about 6% relative error. It is noted that the discrepancy in the number of tin in formula unit obtained from the XRD 17(1)and the SEM 18(1) was also indicated in case of Er/Sn ratio in the single crystal study [28]. In our case the discrepancy does not exceed 2 standard deviations and can be explained within a statistical error. An alternative explanation might indicate a formation of minimal quantities of secondary phases with a higher Sn content, which are picked up by the SEM but not by the XRD. Let us now look at the refined values of ADPs, which are selectively presented in Fig. 15. It must be noted that much better description could be obtained from anisotropic ADPs as it was done in the single crystal study [28] but they are very difficult to obtain from a limited number of reflections available from powder diffraction. The lowest ADP value ≈3 $Å^2$ is observed for the Rh1 and is slowly increasing with the temperature. This behaviour is consistent with a well localised site, without positional disorder, which random displacements are predominantly defined by a thermal motion. The high stability of the Rh1 was one of the reasons for selecting Rh1 as the basis of the structural model presented in Fig. 12. At the other end of the scale is Sn4, which has the highest value of ADP ≈15 $Å^2$ because it is loosely bound to the framework. Unexpectedly its ADP starts to decrease above 375 K, which indicates that this high ADP value has two components: 1) a monotonically increasing thermal motion and 2) a static disorder, which starts to decrease at 375 K. The decrease of Sn4 ADPs at

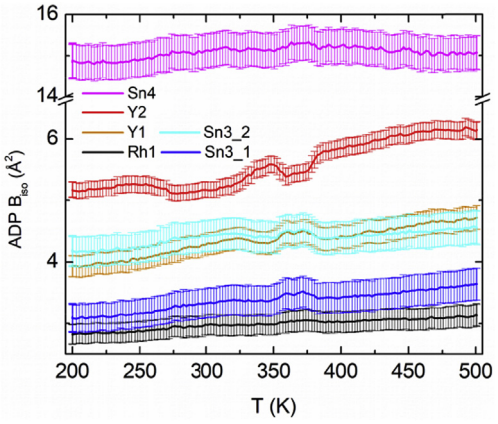

Fig. 15. Temperature dependence of the isotropic Atomic Displacement Parameters (ADPs) for selected atoms. The largest change is observed in the ADP of Y2 but is also mirrored other atoms like in Y1, Sn3_1 or Sn3_2. For all parameters see the SI.

higher temperatures due to a decrease of a static disorder can be understood in term of annealing, which should thermally average the whole structure. The time scale of this relaxation is of the order of the 20 s time interval between the datasets. Additionally, the higher thermal motion of the framework will effectively shrink the Sn4 cage increasing its confinement. The non-thermal character of Sn4 displacements was also visible in analysis of the single crystal data for the Er-based compound by Hodeau *et al.* [28] where they had to remove symmetry restrains from anisotropic β_{ij}s for Sn4 in order to get a reasonable fit. A solution which would not violate the symmetry would require a use of a split Sn4 site, which simulated positional disorder. In our case, with limited powder XRD data it is practically unfeasible to refine an anisotropic ADP or a split site. The second highest value of ADP $\approx$ 5.5 Å^2 is observed for Y2, which is semi-isolated [54] from the framework. The two drops in the value of Y2 ADP at 275 K and 350 K are correlated to flattening of Sn4 ADP between 275 K and 350 K and then by its decrease. Both effects can be attributed to a varying interaction of Y2 with the lattice. The change in coupling is also reflected in the framework when we notice an anti-correlation with ADPs of Sn3_(1,2), Y1 and Rh2 (omitted for clarity) (Fig. 15), which points towards Y2 being a semi-correlated *rattler*. When it attaches itself to the framework (the nearest neighbour is Rh2 at 3 Å) its ADP decreases but the framework ADPs increase and *vice versa*.

Let us discuss temperature dependence of selected fractional coordinates, which are presented in Fig. 16 for the ab-plane and Fig. 17 for the c-axis (All plots are available in Appendix A). In order to bring the changes to the same scale, the figures present variation of fractional coordinates vs their values at 200 K.

When the temperature increases, the fractional coordinates remain unchanged until around 300 K, when some atoms start to deviate from their positions predominantly in the ab-plane. The most active site is Y2 but a clear change is also observed for Sn3_3 especially in the y-coordinate. A weaker effect is observed for Rh2 and Sn3_2. This effect appears about 25 K higher than the changes in ADPs therefore one can say that the coupling of Y2 first modifies the thermal motion (ADPs) of atoms and then results in change of their average positions. Remarkably, the position of Sn4 is not influenced at this temperature, which suggests that it is inactive in this transition. The second class of atomic movements is observed around 350 K and affects Sn3_1, Sn3_2, Sn3_3, Sn3_4 and Sn4(y), which practically involves the whole structure. The fractional position of Sn4 basically remains constant, which corresponds to the decrease of its ADP and agrees with the annealing hypothesis. To sum up, the variations observed in refined parameters indicate that the Y2 is the main atom responsible for the transition around 275 K – 300 K, which is connected with its increased interaction with the framework and shifts atoms mostly in the ab-plane. In turn, at 350 K all directions become active and the main role seems to be played by the Sn4, which is affected by a static positional disorder below this temperature. Finally, let us discuss a possible connection between the changes seen in the XRD experiments with the development of a dynamical CDW phase. The canonical static CDW is usually connected with a long range ordered structure and a suppression of the SC state. It has been speculated for a long time [55,56] and recently proven experimentally [57] that CDW might also have a short-range dynamical character, which extends well above the SC and pseudo-gap opening temperatures. This is also not a local pair-density wave [58] type CDW, which in the picture presented by Arpaia *et al.* would be equivalent to a quasi-critical 2D CDW. In this context, the transition around 340 K–360 K (as seen from susceptibility in Fig. 4 and XRD in Fig. 13) might be connected with the onset of the dynamical CDW in a way similar to T_{HT} observed in $Ca_{0.2}La_{2.8}Rh_4Sn_{13}$ [11]. Below this temperature there are several regions with anomalous responses in different physical properties: (a) around 280 K (in 5 cycles of resistance shown in Fig. 7 and the inset), (b) around 300 K in the cell volume in Fig. 13, (c) around 300 K in the atomic coordinates displayed in Figs. 16 and 17, and finally (d) 160 K in the specific heat Fig. 8.

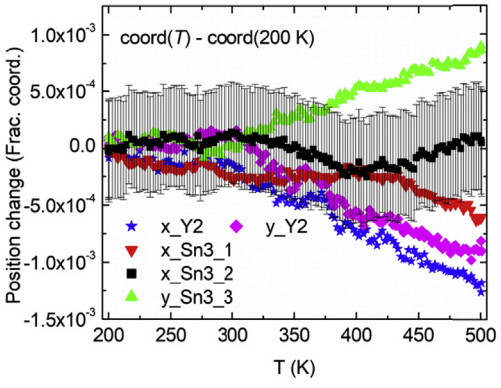

Fig. 16. Atomic coordinates in the *ab*-plane plotted relatively to their 200 K values. Atomic movement starts to develop around 275 K with the leading role of Y2. For clarity fit uncertainty is plotted only for one coordinate.

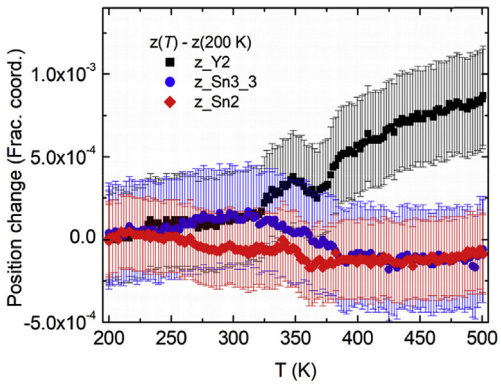

Fig. 17. Temperature dependence of selected fractional coordinates along the *c*-axis plotted vs values refined at 200 K.

In this context, the transitions around 300 K (around 25 meV) are most likely connected to the aforementioned pinning of the dynamic CDW on defects in the structure (Cf. Refs. [59,60]). This picture is supported by the systematic decrease of the anomaly under subsequent heating and cooling ramps (Fig. 7, inset), when the structure becomes *more average*. On top of the proposed pinning, below 300 K, we have suppressed movement of atomic positions (this includes vacancies), which oscillate around their average values refined at 200 K (Figs. 16 and 17). While comparing the resistance to the XRD it must be noted that only the first ($B = 0$ T) heating ramp in the resistance (Fig. 7) is equivalent to the XRD runs which were collected on the first heating of a fresh piece of the sample. At this moment, we can only compare this result to the previous studies [11] and references therein for $La_3Rh_4Sn_{13}$, similar sequence of transitions was also observed for $Ca_{0.2}La_{2.8}Rh_4Sn_{13}$. The $La_3Rh_4Sn_{13}$ also displays a precursor transition at $T_{HT} = 311$ K, which is clearly connected to a local disorder but contrary to Y–Rh–Sn system, it locks into a long range ordered CDW-type superstructure at $T^* = 280$ K. This transition is still debated between a phonon soft mode and CDW like anomaly but most likely both mechanisms are involved. In the case of $Y_5Rh_6Sn_{18}$, the nonstoichiometry and disorder suppress the formation of a long range CDW superstructure.

At $T_D = 160$ K the system is most likely entering the quasi-critical region of the CDW [57,58]. but this temperature region was not achievable during the XRD measurement.

3.4. Electronic band structure of $Y_5Rh_6Sn_{18}$ near the Fermi level; a possible Fermi surface nesting and charge-density wave formation

A variety of properties of $Y_5Rh_6Sn_{18}$ documented by our investigations may indicate some peculiar character of band structure near Fermi energy and shape of Fermi surface. Band structure displayed in Fig. 18 along high-symmetry lines possess dispersive electronic states near the Fermi level, which is consistent with the metallic conductivity of $Y_5Rh_6Sn_{18}$, shown in Fig. 7. Furthermore, the character of the band structure near Fermi level and the shape of Fermi surface (Fig. 19) can be linked to the occurrence of charge density waves.

It is worth note that investigated compound, for it's symmetry, belongs to a special class of non-symmmorphic materials. Recent investigations have shown that the bulk materials with non-symmorphic space groups may exhibit unusual properties of their electronic structure [62,63] resulted from the band degeneracies entailed by non-symmmorphic symmetry. Characteristic property of band structure of such materials is the presence of Dirac cones and Dirac nodes [62]. Depending on the filling level of the bands the non-symmorphic materials may undergo Mott transition [64] or show the presence of charge density waves associated with Peierls transition [65]. The band structure presented in Fig. 18 reveals the presence of several Dirac cone like shapes (e.g. on $\Gamma - Z - \Sigma - N$ symmetry lines). The property of band structure may be related to the occurrence of CDW in investigated compound.

Another property of the band structure which may indicate the occurrence of CDW is the presence of nested portions of the Fermi surface [66]. Fig. 19 shows the Fermi surface for a four bands calculated without SOC.

Only three bands (1033, 1034 and 1034) have pronounced Fermi surface. For all of them the nesting effect may be ascribed but with different directions of nesting vectors. While for the 1033 and 1034 bands the nesting vector lays along the $\vec{b}_3$ direction, the 1035 band shows the nesting along the $\vec{b}_1$ direction. Although, according to Johannes and Mazin work [67] the presence of nesting effects of Fermi surface is not a unique criterion for the occurrence of charge density waves, the nesting visible on Fig. 19 and characteristic Dirac cones present in band structure (Fig. 18) support interpretation of our experimental findings assuming presence of CDW in investigated material. In very recent structural investigations of the $R_3M_4Sn_{13}$-type compounds (R = La or Ce [11,68]) the Rietveld refinement proved the high temperature structural transition $T_{HT} \sim$ 350 K connected to atomic disorder (ADPs), which subsequently leads to the long range superstructure at $T^\star$ and the subtle effects observed at $T_D \sim 150$ K leave no structural signatures. The T_D has been suggested to be associated with a CDW–type instability (c.f. [69]), and $T_D < T^\star < T_{HT}$. In the area of large disorder, structural deformations of T_{HT} or T_D-type are not visible [11]. This is probably the case of $Y_5Rh_6Sn_{18}$, while at T_D are clear anomalies in the specific heat shown in Fig. 8*a* and susceptibility data (in Figs. 4 and 5).

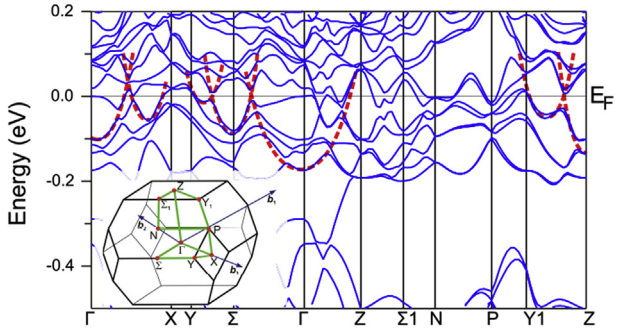

Fig. 18. Calculated band structure of $Y_5Rh_6Sn_{18}$ with SOC along high symmetry lines shown in the inset. Inset presents the Brillouine zone of BCT_2 structure with high symmetry points and lines [61]. Green lines depict the path used for band structure plot. The intersections of red parabola at the Fermi level (along $Y-\Sigma-\Gamma$ and $Y1 - Z$ lines) show electron states dispersion relations similar to a Dirac-cone. (For interpretation of the references to colour in this figure legend, the reader is referred to the Web version of this article.)

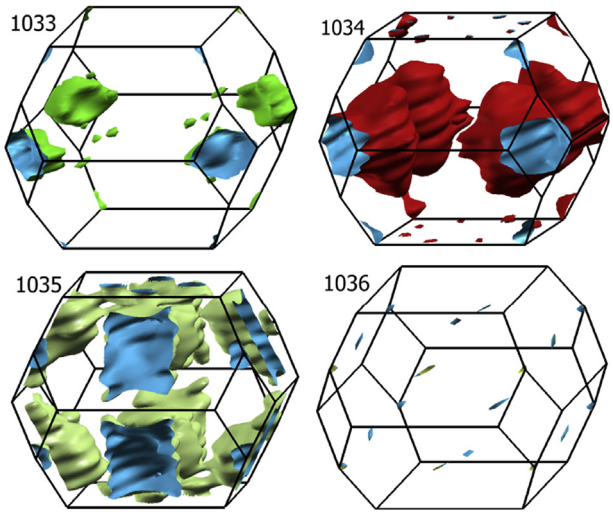

Fig. 19. Fermi surfaces of $Y_5Rh_6Sn_{18}$ with indicated band's number. Orientation of BZ is consistent with that shown in the inset of Fig. 18.

4. Concluding remarks

Our intention was to obtain $Y_3Rh_4Sn_{13}$ with a cubic $Yb_3Rh_4Sn_{13}$-type structure (space group $Pm\bar{3}n$). We showed, however, that this stoichiometry is not possible for a ternary system Y–Rh–Sn. However, it is possible to obtain a similar skutterudite-related $Y_5Rh_6Sn_{18+\delta}$ compound having a cage-like structure, which crystallises in tetragonal structure with the space group $I4_1/acd$ (Z = 8), and exhibits superconductivity as does equivalent cubic system $La_3Rh_4Sn_{13}$ of $Yb_3Rh_4Sn_{13}$-type structure.

We have investigated the superconducting state in $Y_5Rh_6Sn_{18}$ by using electric transport, magnetic, and specific heat experimental techniques. All experiments were performed on the same polycrystalline sample, whose high quality is evidenced by microanalysis and XRD studies. The measurements reveal that $Y_5Rh_6Sn_{18}$ is BCS superconductor with superconducting phase transition at 3.08 K. Anomalous behaviour observed in electronic specific heat $C(T)/T$ and $H_{c2}(T)$ provides evidence for two superconducting gap behaviour. This phenomena is also supported by the *ab initio* band structure calculations, which predict the presence of *s*, *p*, and *d* electron states at the Fermi level. Based on experimental data we determined some fundamental thermodynamic parameters characteristic of the dirty superconductor of type II. In a dirty limit we found the coherence length $\xi > l$, then the WHH theory well approximates the temperature dependence of the upper critical field H_{c2} in the $H - T$ diagram within the two-band model.

The structural analysis has shown that the anomalies clearly visible in temperature dependencies of various thermodynamic quantities at $T \sim 300$ and ~ 350 K do not change the symmetry of the system but the reason for the observed anomalies is a thermal lattice relaxation process. At 300 K mostly Y2 and Sn3_3 atoms start to deviate from their positions determined by the minimum energy of the crystal at low temperatures. A change of the character of thermal motion to more collective (correlated rattler) is observed with the increase of *T*. At ~ 350 K Sn4 atoms tend to occupy the equilibrium position due to thermal activation-like behaviour. There is some structural analogy to cubic $La_3Rh_4Sn_{13}$ system, where

increase of atomic displacements with thermal noise begins at about 250 K and finally is completed at around 300 K [11]. However, for the system of 3 : 4 : 13 compounds there is evidence of structural transition, which is not explicitly found for $Y_5Rh_6Sn_{18}$.

Declaration of competing interest

The authors declare that they have no known competing financial interests or personal relationships that could have appeared to influence the work reported in this paper.

Acknowledgments

A.Ś. thanks to the Kosciuszko Foundation (New York) for the partial support of the research. M.M.M. acknowledges support by the National Science Centre (Poland) under grant DEC-2018/29/B/ST3/01892. P.Z. would like to thank the SNBL(ESRF) staff for their help in collecting the data.

Appendix A

In this Appendix we show temperature dependence of atomic parameters for atoms occupying the unit cell of $Y_5Rh_6Sn_{18}$ (see Table 1). Columns represent respectively fractional coordinate positions [x, y, z], a chemical site occupation factor (SOF), an isotropic atomic displacement parameter (ADP) B_{iso}.

Label	x	y	z	SOF	Biso
Rh1	Fixed at 0.0 by Wyckoff position	Fixed at 0.25 by Wyckoff position	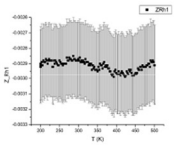	Fixed to 1	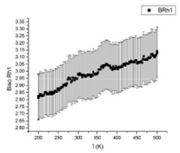
Rh2	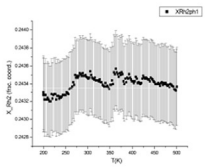	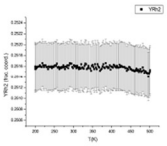	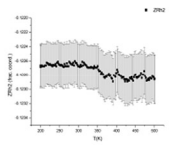	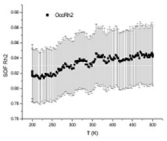	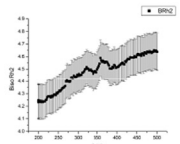
Y1	Fixed at 0.0 by Wyckoff position	Fixed at 0.25 by Wyckoff position	Fixed at 0.125 by Wyckoff position	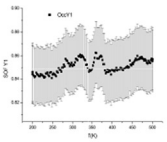	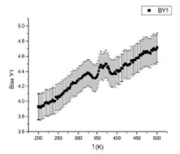
Y2	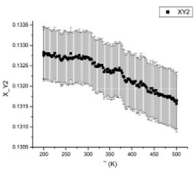	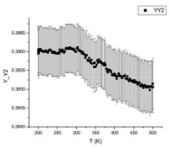	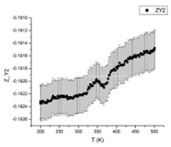	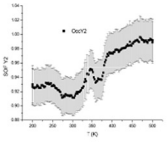	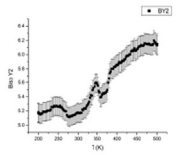
Sn2	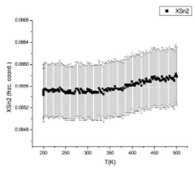	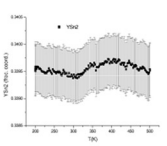	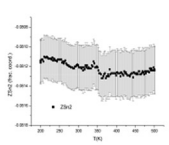	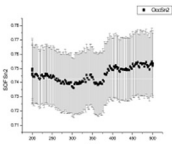	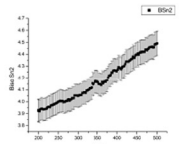
Sn3_1	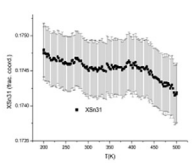	Fixed at x+0.25 by Wyckoff position	Fixed at 0.125 by Wyckoff position	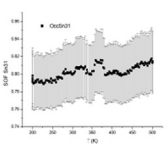	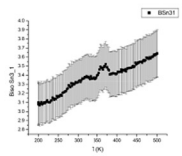

Fig. 20. Plots of atomic parameters from Rietveld refinement in the temperature region 200 K and 500 K (in all plots 200 K $\leq T \leq$ 500 K scale is linear.).

References

[1] R. Kurleto, J. Goraus, M. Rosmus, A. Ślebarski, P. Starowicz, Eur. Phys. J. 92 (2019) 192.
[2] T.-S. Nam, Ch-J. Kang, D.C. Ryu, J. Kim, H. Kim, K. Kim, B.I. Min, Phys. Rev. B 99 (2019) 125115.
[3] D. Kaczorowski, A.V. Gribanov, S.F. Dunaev, J. Alloy. Comp. 742 (2018) 594–600.
[4] E.D. Bauer, A. Ślebarski, E.J. Freeman, C. Sirvent, M.B. Maple, J. Phys. Condens. Mater. 13 (2001) 4495.
[5] G.R. Stewart, Rev. Mod. Phys. 73 (2001) 797–855.
[6] Sung-Sik Lee, Annu. Rev. Condens. Matter Phys. 9 (2018) 227–244.
[7] J. Huang, L. Zhao, C. Li, Q. Gao, J. Liu, Y. Hu, Y. Xu, Y. Cai, D. Wu, Y. Ding, C. Hu, H. Zhou, X. Dong, G. Liu, Q. Wang, S. Shang, Z. Wang, F. Zhang, Q. Peng, Z. Xu, C. Chen, X. Zhou, Sci. Bull. 64 (2019) 11–19.
[8] J.P. Remeika, G.P. Espinosa, A.S. Cooper, H. Barz, J.M. Rowel, D.B. McWhan, J.M. Vandenberg, D.E. Moncton, Z. Fizk, L.D. Woolf, H.C. Hamaker, M.B. Maple, G. Shirane, W. Thomlinson, Solid State Commun. 34 (1980) 923–926.a J.L. Hodeau, M. Marezio, J.P. Remeika, C.H. Chen, *ibid.* 42 (1982) 97-102.
[9] A. Ślebarski, J. Goraus, Physica B 536 (2018) 165–168.
[10] A. Ślebarski, M. Fijałkowski, M.M. Maśka, M. Mierzejewski, B.D. White, M.B. Maple, Phys. Rev. B 89 (2014) 125111.
[11] A. Ślebarski, P. Zajdel, M. Fijałkowski, M.M. Maśka, P. Witas, J. Goraus, Y. Fang, D.C. Arnold, M.B. Maple, New J. Phys. 20 (2018) 103020.
[12] The *D*-Electron Correlations in the Series of $La_M3_4Sn_{13}$ Skutterudite-Related Compounds Were Experimentally Documented and Discussed in Ref. [13].
[13] A. Ślebarski, J. Goraus, P. Witas, L. Kalinowski, M. Fijałkowski, Phys. Rev. B 91 (2015), 035101.
[14] M.B. Maple, P.-C. Ho, V.S. Zapf, N.A. Frederick, E.D. Bauer, W.M. Yuhasz, F.M. Woodward, J.W. Lynn, J. Phys. Soc. Jpn. Suppl. 71 (2002) 23–28.
[15] R. Vollmer, A. Faißt, C. Pfleiderer, H.v. Löhneysen, E.D. Bauer, P.-C. Ho, V. Zapf, M.B. Maple, Phys. Rev. Lett. 90 (2003), 057001.
[16] G. Seyfarth, J.P. Brison, M.-A. Méasson, D. Braithwaite, G. Lapertot, J. Flouquet, Phys. Rev. Lett. 97 (2006) 236403.
[17] M.-A. Méasson, D. Braithwaite, G. Lapertot, J.-P. Brison, J. Flouquet, P. Bordet, H. Sugawara, P.C. Canfield, Phys. Rev. B 77 (2008) 134517.
[18] A. Bianchi, R. Movshovich, M. Jaime, J.D. Thompson, P.G. Pagliuso, J.L. Sarrao, Phys. Rev. B 64 (2001), 220504(R).
[19] B.M. Andersen, A. Melikyan, T.S. Nunner, P.J. Hirschfeld, Phys. Rev. B 74 (2006), 060501(R).
[20] T. Cren, D. Roditchev, W. Sacks, J. Klein, J.-B. Moussy, C. Deville-Cavellin, M. Laguës, Phys. Rev. Lett. 84 (2000) 147–150.
[21] L. Gastaldo, P. Manfrinetti, F. Gatti, G. Gallinaro, D. Pergolesi, M.R. Gomes, M. Razeti, S. Dussoni, P. Repetto, R. Valle, Nucl. Instrum. Methods Phys. Res. A 520 (2004) 224–226.
[22] N. Kase, K. Inoue, H. Hayamizu, J. Akimitsu, J. Phys. Soc. Jpn. 80 (2011) SA112.
[23] Z. Zhang, Y. Xu, C.N. Kuo, X.C. Hong, M.X. Wang, P.L. Cai, J.K. Dong, C.S. Lue, S.Y. Li, Supercond. Sci. Technol. 28 (2015) 105008.
[24] A. Bhattacharyya, D. Adroja, N. Kase, A. Hillier, J. Akimitsu, A. Strydom, Sci. Rep. 5 (2015) 12926.
[25] J.L. Hodeau, M. Marezio, J.P. Remeika, C.H. Chen, Solid State Commun. 42 (1982) 97–102.
[26] J.C. Slater, J. Chem. Phys. 41 (1964) 3199–3204.
[27] G. Venturini, M. Meot-Meyer, B. Malaman, B. Rodues, J. Less Common. Met. 113 (1985) 197–204.
[28] J.L. Hodeau, M. Marezio, J.P. Remeika, Acta Crystallogr. B 40 (1984) 26–38.
[29] S. Miraglia, J.L. Hodeau, M. Marezio, H.R. Ott, J.P. Remeika, Solid State Commun. 52 (1984) 135–137.
[30] A. Ślebarski, J. Goraus, M.M. Maśka, P. Witas, M. Fijałkowski, C.T. Wolowiec, Y. Fang, M.B. Maple, Phys. Rev. B 93 (2016) 245126.
[31] K. Suyama, K. Iwasa, Y. Otomo, K. Tomiyasu, H. Sagayama, R. Sagayama, H. Nakao, R. Kumai, Y. Kitajima, F. Damay, J.M. Mignot, A. Yamada, T.D. Matsuda, Y. Aoki, Phys. Rev. B 97 (2018) 235138.
[32] P. Bordet, D.E. Cox, G.P. Espinosa, J.L. Hodeau, M. Marezio, Solid State Commun. 78 (1991) 359–366.
[33] V. Dyadkin, P. Pattison, V. Dmitriev, D. Chernyshov, J. Synchrotron Radiat. 23 (2016) 825–829.
[34] H.M. Rietveld, J. Appl. Crystallogr. 2 (1969) 65–71.
[35] J. Rodriguez-Carvajal, Physica B 192 (1993) 55–69.
[36] P. Blaha, K. Schwarz, G.K.H. Madsen, D. Kvasnicka, J. Luitz, R. Laskowski, F. Tran, L.D. Marks, WIEN2k, an Augmented Plane Wave + Local Orbitals Program for Calculating Crystal Properties, Karlheinz Schwarz, Technische Universität Wien, Austria, 2001, ISBN 3-9501031-1-2.
[37] D.J. Singh, L. Nordstrom, Plane Waves, Pseudopotentials, and the LAPW Method, second ed., Springer Science, 2006, ISBN 978-0-387-28780-5.
[38] J.P. Perdew, A. Ruzsinszky, G.I. Csonka, O.A. Vydrov, G.E. Scuseria, L.A. Constantin, X. Zhou, K. Burke, Phys. Rev. Lett. 100 (2008) 136406.
[39] M. Gamża, W. Schnelle, A. Ślebarski, U. Burkhardt, R. Gumeniuk, H. Rosner, J. Phys. Condens. Matter 20 (2008) 395208.
[40] A. Ślebarski, J. Goraus, Phys. Rev. B 88 (2013) 155122.
[41] T.P. Orlando, E.J. McNiff Jr., S. Foner, M.R. Beasley, Phys. Rev. B 19 (1979) 4545–4561.
[42] G.M. Eliashberg, Sov. Phys. JEPT 11 (1960) 696–702;
a G.M. Eliashberg, Sov. Phys. JEPT 12 (1961) 1000–1002.
[43] W.L. McMillan, Phys. Rev. 167 (1968) 331–344.
[44] R.C. Dynes, Solid State Commun. 10 (1972) 615–618.
[45] U.S. Kaluarachchi, W. Xie, Q. Lin, V. Taufour, S.L. Bud'ko, G.J. Miller, P.C. Canfield, Phys. Rev. B 91 (2015) 174513.
[46] A. Ślebarski, M.M. Maśka, M. Fijałkowski, C.A. McElroy, M.B. Maple, J. Alloy. Comp. 646 (2015) 866–872.
[47] V.V. Schmidt, in: P. Müllerand, A.V. Ustinov (Eds.), The Physics of Superconductors, Springer, Berlin, 1977.
[48] E. Helfand, N.R. Werthamer, Phys. Rev. Lett. 13 (1964) 686–688;
a N.R. Werthamer, E. Helfand, P.C. Hohenberg, Phys. Rev. 147 (1966) 295–302.
[49] E. Helfand, N.R. Werthamer, Phys. Rev. 147 (1966) 288–294.
[50] P.G. de Gennes, Phys. Kondens. Mater. 3 (1964) 79–90;
a K. Maki, Physics 1 (1964) 21–30;
b P.G. DeGennes, Superconductivity in Metals and Alloys, Benjamin, New York, 1966.
[51] J.P. Carbotte, Rev. Mod. Phys. 62 (1990) 1027–1157.
[52] A. Gurevich, Phys. Rev. B 67 (2003) 184515.
[53] S. Grazulis, D. Chateigner, R.T. Downs, A.T. Yokochi, M. Quiros, L. Lutterotti, E. Manakova, J. Butkus, P. Moeck, A. Le Bail, J. Appl. Crystallogr. 42 (2009) 726–729.
[54] Here 'semi-Isolated' Means Not Closely (<2.8 Å) Connected to the Rest of the Framework but the NN Is Rh2 at the Distance Close to 3.0 Å), in Fig. 12(b).
[55] L. Benfatto, S. Caprara, C. Di Castro, Eur. Phys. J. 17 (2000) 95–102.
[56] S. Caprara, C. Di Castro, G. Seibold, M. Grilli, Phys. Rev. B 95 (2017) 224511.
[57] R. Arpaia, S. Caprara, R. Fumagalli, G. De Vecchi, Y.Y. Peng, E. Andersson, D. Betto, G.M. De Luca, N.B. Brookes, F. Lombardi, M. Salluzzo, L. Braicovich, C. Di Castro, M. Grilli, G. Ghiringhelli, Science 365 (6456) (2019) 906–910.
[58] M. Leroux, V. Mishra, J.P.C. Ruff, H. Claus, M.P. Smylie, Ch Opagiste, P. Rodiere, A. Kayani, G.D. Gu, J.M. Tranquada, W.-K. Kwok, Z. Islam, U. Welp, Proc. Natl. Acad. Sci. 116 (2019) 10691–10697.
[59] C.S. Lue, Y.-K. Kuo, F.H. Hsu, H.H. Li, H.D. Yang, P.S. Fodor, L.E. Wenger, Phys. Rev. B 66 (2002), 033101.
[60] L. Mendonca-Ferreira, F.B. Carneiro, M.B. Fontes, E. Baggio-Saitovich, L.S.I. Veiga, J.R.L. Mardegan, J. Strempfer, M.M. Piva, P.G. Pagliuso, R.D. dos Reis, E.M. Bittar, J. Alloy. Comp. 773 (2019) 34–39.
[61] W. Setyawan, S. Curtarolo, Comput. Mater. Sci. 49 (2010) 299–312.
[62] S.M. Young, S. Zaheer, J.C.Y. Teo, C.L. Kane, E.J. Mele, A.M. Rappe, Phys. Rev. Lett. 108 (2012) 140405.
[63] S.M. Young, C.L. Kane, Phys. Rev. Lett. 115 (2015) 126803.
[64] N.J. Mott, J. Solid State Chem. 88 (1990) 5–7.
[65] J.A. Wilson, F. Di Salvo, S. Mahajan, Adv. Phys. 24 (1975) 117–201.
[66] Y.-D. Chuang, A.D. Gromko, D.S. Dessau, T. Kimura, Y. Tokura, Science 292 (2001) 1509–1513.
[67] M.D. Johannes, I.I. Mazin, Phys. Rev. B 77 (2008) 16535.
[68] C.N. Kuo, W.T. Chen, C.W. Tseng, C.J. Hsu, R.Y. Huang, F.C. Chou, Y.K. Kuo, C.S. Lue, Phys. Rev. B 97 (2018), 094101.
[69] Y. Otomoto, K. Iwasa, K. Suyama, K. Tomiyasu, H. Sagayama, R. Sagayama, H. Nakao, R. Kumai, Y. Murakami, Phys. Rev. B 94 (2016), 075109.